BOLETIN DE LA SOCIEDAD ESPAÑOLA DE
Cerámica y Vidrio
www.elsevier.es/bsecv

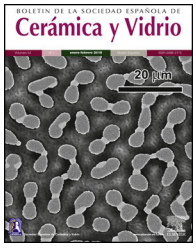

Al^{3+} doping reduces the electron/hole recombination in photoluminescent copper ferrite ($CuFe_{2-x}Al_xO_4$) nanocrystallites

Faraj Ahmad Abuilaiwi[a,b,*], *Muhammad Awais*[c], *Umair Yaqub Qazi*[a,d], *Farman Ali*[e], *Adeel Afzal*[a,b,f,*]

[a] *Department of Chemistry, College of Science, University of Hafr Al Batin, PO Box 1803, Hafr Al Batin 39524, Saudi Arabia*
[b] *Affiliated Colleges at Hafr Al Batin, King Fahd University of Petroleum and Minerals, PO Box 1803, Hafr Al Batin 31991, Saudi Arabia*
[c] *Department of Industrial Engineering, College of Engineering, Taibah University, Saudi Arabia*
[d] *Division of Nanomaterials and Chemistry, Hefei National Laboratory for Physical Sciences at Microscale, University of Science and Technology of China, Hefei, Anhui 230026, PR China*
[e] *Department of Chemistry, Hazara University, Mansehra, Khyber Pakhtunkhwa 21300, Pakistan*
[f] *Dipartimento di Chimica, Università degli Studi di Bari "Aldo Moro", Via Orabona 4, 70126 Bari, Italy*

ARTICLE INFO

Article history:
Received 28 May 2020
Accepted 19 November 2020
Available online 14 December 2020

Keywords:
Al doping
Copper ferrite
Optical bandgap
Nanocrystals
Photoluminescence spectroscopy

ABSTRACT

Nanocrystalline copper ferrite shows distinct photocatalytic properties, but it suffers from a high recombination rate of photogenerated electrons (e^-) and holes (h^+) due to its narrow bandgap. Herein, Al^{3+} doping is shown to reduce the (e^-/h^+) recombination rate and improve the charge carriers' availability in doped $CuFe_{2-x}Al_xO_4$ ($0 \le x \le 1$) nanoparticles produced by a solid-state, mechanochemical process. $CuFe_{2-x}Al_xO_4$ ($0 \le x \le 1$) nanoparticles exhibit the growth of a nanocrystalline cubic spinel lattice when annealed at 1000 °C. The lattice parameter is reduced by Al^{3+} doping due to the smaller ionic radius of Al^{3+} ions substituting bigger Fe^{3+} ions. However, a higher degree of sintering and greater crystallite size are observed for Al^{3+} doped samples. The surface morphology and topography also reveal an increase in the particle size, but significantly narrow size distribution and greater homogeneity. The effect of Al^{3+} doping on the optical properties of $CuFe_{2-x}Al_xO_4$ ($0 \le x \le 1$) nanoparticles is demonstrated by a decrease in the photoluminescence signal that is attributed to the lower rate of (e^-/h^+) recombination. Thus, Al^{3+} doping increases transition time and improves the availability of charge carriers for potential photocatalytic applications.

* *Corresponding authors.*
E-mail addresses: faraj@uhb.edu.sa (F. Ahmad Abuilaiwi), aa@aafzal.com (A. Afzal).
https://doi.org/10.1016/j.bsecv.2020.11.007

El dopaje con Al^{3+} reduce la recombinación de electrones/agujeros en nanocristales de ferrita de cobre ($CuFe_{2-x}Al_xO_4$) fotoluminiscentes

Palabras clave:
Al dopaje
Ferrita de cobre
Banda óptica
Nanocristales
Espectroscopia de fotoluminiscencia

RESUMEN

La ferrita de cobre nanocristalino muestra propiedades fotocatalíticas distintas, pero sufre de una alta tasa de recombinación de electrones fotogenerados (e^-) y agujeros (h^+) debido a su estrecha banda prohibida. Aquí, se muestra que el dopaje Al^{3+} reduce la tasa de recombinación (e^-/h^+) y mejora la disponibilidad de los portadores de carga en nanopartículas de $CuFe_{2-x}Al_xO_4$ ($0 \le x \le 1$) dopadas producidas por un proceso mecanoquímico de estado sólido. Las nanopartículas de $CuFe_{2-x}Al_xO_4$ ($0 \le x \le 1$) exhiben el crecimiento de una red de espinela cúbica nanocristalina, cuando se recocen a 1000 °C. El parámetro de red se reduce por el dopaje Al^{3+} debido al radio iónico más pequeño de los iones Al^{3+} que sustituyen los iones Fe^{3+} más grandes. Sin embargo, se observa un mayor grado de sinterización y un mayor tamaño de cristalito para las muestras dopadas con Al^{3+}. La morfología y la topografía de la superficie también revelan un aumento en el tamaño de partícula, pero una distribución del tamaño significativamente más estrecha y una mayor homogeneidad. El efecto del dopaje Al^{3+} sobre las propiedades ópticas de las nanopartículas de $CuFe_{2-x}Al_xO_4$ ($0 \le x \le 1$) se demuestra por una disminución en la señal de fotoluminiscencia que se atribuye a la tasa más baja de recombinación (e^-/h^+). Por lo tanto, el dopaje Al^{3+} aumenta el tiempo de transición y mejora la disponibilidad de portadores de carga para posibles aplicaciones fotocatalíticas.

Introduction

Cubic spinel ferrites are photoactive materials that can be easily photoexcited under visible light to generate electrons (e^-) and holes (h^+): the active sites for the redox processes [1]. Due to their excellent photocatalytic properties, spinel ferrites have attracted massive research in different fields of catalysis [2–5]. Their photocatalytic efficiency is mainly a consequence of their narrow bandgap ~2.0 eV [6]; which makes them efficient photocatalysts capable of utilizing visible solar energy. Among these spinel ferrites, nanocrystalline copper ferrite ($CuFe_2O_4$) has the lowest bandgap 1.32 eV [1]. Therefore, spinel $CuFe_2O_4$-based photocatalytic materials have found applications in solar water splitting [7,8], CO_2 reduction [9,10], and degradation of contaminants [11,12].

However, $CuFe_2O_4$ nanostructures also suffer from a high (e^-/h^+) recombination rate due to their narrow bandgap, which inhibits charge availability and photo-response [10]. To improve the photoactivity of $CuFe_2O_4$, nanocomposites are developed by combining $CuFe_2O_4$ nanoparticles with quantum dots, polymers, graphene, or ceramics [9,10,12,13]. The synergistic combination of $CuFe_2O_4$ nanoparticles with different materials improves the charge separation and reduces the (e^-)/(h^+) recombination rate in $CuFe_2O_4$. The processing of nanocomposites, however, requires additional steps, materials, and cost.

An alternative, cost-effective, and uncomplicated approach involves doping of $CuFe_2O_4$ nanoparticles with different di- or trivalent metals such as Zn^{2+} and Ce^{3+} [14,15]. Doping can substantially alter the crystal structure, ionic distribution, and optical properties of $CuFe_2O_4$ nanoparticles [16]. This article presents a straightforward route for mechanochemical synthesis of Al^{3+} doped $CuFe_2O_4$ solid solutions with a chemical formula: $CuFe_{2-x}Al_xO_4$ (where, $x = 0$, 0.2, 0.4, 0.6, 0.8, and 1.0; thus, written as ($0 \le x \le 1$)). These $CuFe_{2-x}Al_xO_4$ ($0 \le x \le 1$) nanoparticles are prepared via a solvent-free and additive-free, solid-state method using a high-energy ball milling (HEBM).

HEBM is a dry powder processing technique that uses mechanical collision and friction energy to produce fine particles and solid solutions [17]. $CuFe_{2-x}Al_xO_4$ ($0 \le x \le 1$) nanoparticles prepared via HEBM are annealed at 1000 °C to yield nanocrystallites. The crystal growth and sintering effects on the lattice parameter, crystallite size, and density are determined by X-ray diffraction analysis. The surface morphology and chemical composition are characterized by a scanning electron microscope equipped with energy-dispersive X-ray spectroscopy. The optical properties are studied by photoluminescence characteristics of $CuFe_{2-x}Al_xO_4$ ($0 \le x \le 1$) nanoparticles.

Materials and methods

Synthesis of $CuFe_{2-x}Al_xO_4$ ($0 \le x \le 1$) nanoparticles

To prepare $CuFe_{2-x}Al_xO_4$ ($0 \le x \le 1$) nanoparticles, iron(III) oxide (Fe_2O_3 nanopowder, <50 nm particle size (BET)), aluminum oxide, (Al_2O_3 nanopowder, <50 nm particle size (TEM)), and copper(II) oxide (CuO nanopowder, <50 nm particle size (TEM)) obtained from Sigma-Aldrich are used. HEBM is used to synthesize $CuFe_{2-x}Al_xO_4$ ($0 \le x \le 1$) nanoparticles with different compositions. A SPEX™ 8000 M Mixer/Mill™ equipped with a 500-cc stainless steel vessel containing stainless steel balls (8 mm diameter) is used for mechanical milling of the

Table 1 – Synthesis of $CuFe_{2-x}Al_xO_4$ ($0 \le x \le 1.0$) nanoparticles: The stoichiometric amounts of CuO, Fe_2O_3, and Al_2O_3 are used to produce 1 g of $CuFe_{2-x}Al_xO_4$ ($0 \le x \le 1.0$) nanoparticles.

x	Balanced chemical equation for $CuFe_{2-x}Al_xO_4$ ($0 \le x \le 1.0$) synthesis
x = 0	$CuO + Fe_2O_3 \rightarrow CuFe_2O_4$
x = 0.2	$10CuO + 9Fe_2O_3 + Al_2O_3 \rightarrow 10CuFe_{1.8}Al_{0.2}O_4$
x = 0.4	$5CuO + 4Fe_2O_3 + Al_2O_3 \rightarrow 5CuFe_{1.6}Al_{0.4}O_4$
x = 0.6	$10CuO + 7Fe_2O_3 + 3Al_2O_3 \rightarrow 10CuFe_{1.4}Al_{0.6}O_4$
x = 0.8	$5CuO + 3Fe_2O_3 + 2Al_2O_3 \rightarrow 5CuFe_{1.2}Al_{0.8}O_4$
x = 1.0	$2CuO + Fe_2O_3 + Al_2O_3 \rightarrow 2CuFeAlO_4$

stoichiometric proportions of Fe_2O_3, Al_2O_3, and CuO. Table 1 shows the balanced chemical equations to determine the stoichiometric amount of CuO, Fe_2O_3, and Al_2O_3 that are used to produce 1 g of $CuFe_2$–xAl_xO_4 nanoparticles with ($x = 0$, 0.2, 0.4, 0.6, 0.8, and 1.0). The steel balls and chemical powders mass ratio is 20 and HEBM is carried out for 5 h at 600 rpm. Finally, the powdered samples are thermally annealed at 1000 °C for 5 h and characterized.

Characterization of $CuFe_{2-x}Al_xO_4$ ($0 \le x \le 1$) nanoparticles

The crystal structure of the as-milled and thermally-annealed $CuFe_{2-x}Al_xO_4$ ($0 \le x \le 1$) nanoparticles is studied with a STOE STADI P X-ray diffractometer (XRD) using a Cu Kα irradiation source ($\lambda = 1.54056$ Å). The samples are scanned in the range of 20–80° with a scan rate of 2°/min. The crystallite size, lattice parameter (a), inter-planar spacing (d_{311}), and X-ray density (ρ_{xrd}) are calculated from the XRD data of annealed $CuFe_{2-x}Al_xO_4$ ($0 \le x \le 1$) nanoparticles [18,19]; that is discussed later.

The microstructure and surface morphology of $CuFe_{2-x}Al_xO_4$ ($0 \le x \le 1$) nanoparticles is studied with a JEOL JSM-6510 scanning electron microscope (SEM). The micrographs are further analyzed with WSxM 4.0 Beta 9.3 and ImageJ 1.52a programs to study the surface topography and measure mean particle/aggregate diameter [20,21]. The elemental composition of $CuFe_{2-x}Al_xO_4$ ($0 \le x \le 1$) nanoparticles is determined with the energy-dispersive X-ray spectroscopy (EDS). The optical properties of $CuFe_{2-x}Al_xO_4$ ($0 \le x \le 1$) nanoparticles are examined by Perkin Elmer LS 45 fluorescence spectrophotometer.

Results and discussion

Structural characterization

The crystal structure of the as-milled $CuFe_{2-x}Al_xO_4$ ($0 \le x \le 1.0$) nanoparticles is characterized by XRD. Fig. 1 shows the XRD patterns of the as-milled $CuFe_{2-x}Al_xO_4$ ($0 \le x \le 1$) nanoparticles along with the JCPDS reference patterns for cubic (card 77-0010 [22]) and tetragonal (card 34-0425 [23]) $CuFe_2O_4$ and reactant metal oxides, i.e. CuO (card 80-1917 [24]), Fe_2O_3 (card 33-0664 [25]), and Al_2O_3 (card 71-1123 [26]). All samples exhibit a characteristic diffraction peaks around 30.5°, 35.8°, and 62.6° 2θ positions, which correspond to the hkl (220), (311), and (440) Miller indices of a spinel ferrite with the

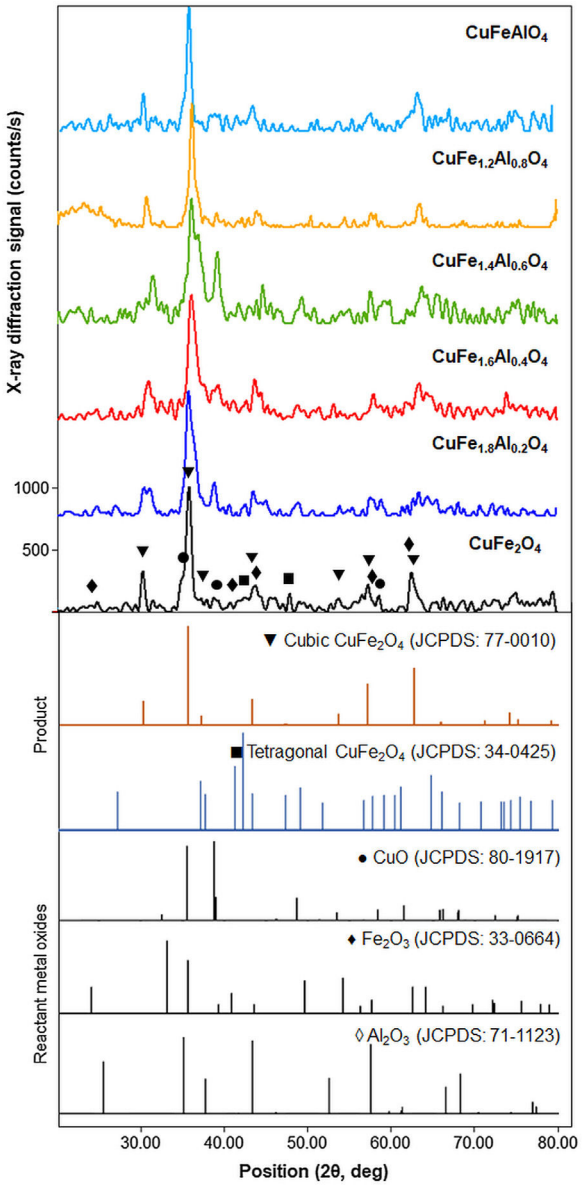

Fig. 1 – XRD patterns of the as-milled $CuFe_{2-x}Al_xO_4$ ($0 \le x \le 1.0$) nanoparticles. The reference patterns for cubic and tetragonal $CuFe_2O_4$ nanoparticles and reacting metal oxides are also included. The existence of the cubic spinel lattice structure as the predominant phase is indicated by the characteristic (220), (311), and (440) diffractions around 30.5°, 35.8°, and 62.6° (2θ position), respectively. The presence of unreacted oxides is also indicated.

Fd3m space group (JCPDS card 77-0010 [22]), respectively. Thus, as-milled $CuFe_{2-x}Al_xO_4$ ($0 \le x \le 1$) nanoparticles indicate the formation of a spinel lattice structure. However, the as-milled $CuFe_{2-x}Al_xO_4$ ($0 \le x \le 1$) nanoparticles are semicrystalline in nature with a significant fraction of amorphous content that is revealed by the noisy pattern. Moreover, the characteristic diffraction peaks are considerably broad with a shoulder or doublet indicating the presence of impurities originating from the unreacted oxides, e.g. CuO and Fe_2O_3, as shown in Fig. 1. Berbenni et al. [27] noticed that $CuFe_2O_4$ crystallized into

a tetragonal lattice at room temperature and they recorded tetragonal to cubic transition at 398 °C.

Marinca et al. [28] studied the structure evolution in ball-milled $CuFe_2O_4$ samples annealed at 600–1000 °C and observed that after 4 h of reactive milling a solid solution of CuO and Fe_2O_3 and a spinel phase is obtained. However, the single cubic spinel phase $CuFe_2O_4$ was formed by annealing at > 600 °C. In this case, XRD patterns of the as-milled samples demonstrate the formation of cubic spinel lattice as the predominant structure, which is well in agreement with the relevant literature [28]. According to a recent study using in situ XRD analysis of $CuFe_2O_4$ nanocrystals, the cubic spinel structure truly evolves at ~1000 °C [29]. Therefore, the as-milled $CuFe_{2-x}Al_xO_4$ ($0 \le x \le 1$) nanoparticles are thermally annealed at 1000 °C to improve the crystallization and purity and their structure is examined after annealing.

XRD patterns of $CuFe_{2-x}Al_xO_4$ ($0 \le x \le 1.0$) nanoparticles annealed at 1000 °C for 5 h are shown in Fig. 2. The reference patterns are also included. The patterns for all $CuFe_{2-x}Al_xO_4$ ($0 \le x \le 1.0$) samples are similar with slight variations in the peak positions except $CuFe_{1.8}Al_{0.2}O_4$. The samples exhibit good crystallinity as indicated by the sharp diffraction peaks. These diffraction peaks are recognized as (220), (311), (222), (400), (422), (511), and (440) planes of the cubic lattice and match well with the cubic spinel copper ferrite (JCPDS card 77-0010) [22]. The data also aligns well with the reported literature for cubic $CuFe_2O_4$ nanoparticles [30,31]. Although all $CuFe_{2-x}Al_xO_4$ ($0 \le x \le 1.0$) samples demonstrate good crystallinity and the formation of a cubic spinel lattice, $CuFe_{1.8}Al_{0.2}O_4$ is an exception. In the case of the $CuFe_{1.8}Al_{0.2}O_4$ sample, broad diffraction peaks with shoulders or superposition of other peaks are observed that may be due to the presence of impurities or unreacted oxides, as shown in Fig. 2. The existence of a secondary phase, i.e. tetragonal $CuFe_2O_4$ is not detected. Thus, it could be attributed to experimental error or poor annealing. However, for other types of $CuFe_{2-x}Al_xO_4$ ($0 \le x \le 1.0$) nanoparticles, there is no detectable peak corresponding to oxide-based impurities, which substantiates the formation of the cubic spinel structure of Al^{3+}-doped copper ferrite nanoparticles.

As shown in Fig. 2, the most intense diffraction corresponds to the (311) plane of the cubic lattice at ~35.8° 2θ position. Fig. 3 shows (311) peak position and width for different types of $CuFe_{2-x}Al_xO_4$ ($0 \le x \le 1.0$) nanoparticles. The position of (311) diffraction varies with the increasing Al^{3+} ratio. The peak shifts to a higher 2θ position as Al^{3+} content increase from 0 to 1, which may be attributed to the smaller size of Al^{3+} ions compared to Fe^{3+} ion [32,33]. The ionic radii of Al^{3+} and Fe^{3+} ions are 0.53 and 0.65 Å, respectively [34]. XRD analysis of the annealed $CuFe_{2-x}Al_xO_4$ ($0 \le x \le 1$) nanoparticles is used to calculate the crystallite size (D), lattice parameter (a), inter-planar spacing (d_{311}), and X-ray density (ρ_{xrd}) of all samples [18]. Table 2 shows the experimentally obtained structural parameters and properties of the annealed $CuFe_{2-x}Al_xO_4$ ($0 \le x \le 1$) nanoparticles.

The interplanar spacing (d_{311}) is calculated from the Bragg's equation (1) [35,36]:

$$\lambda = 2d_{hkl} \sin\theta \quad (1)$$

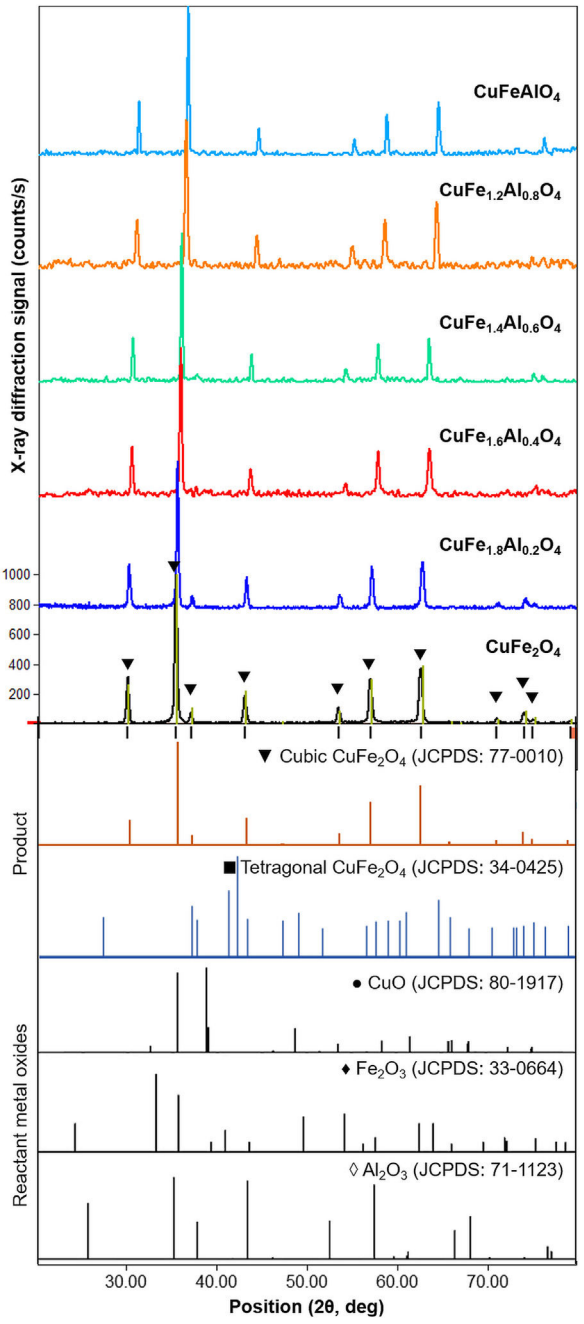

Fig. 2 – XRD patterns of the annealed $CuFe_{2-x}Al_xO_4$ ($0 \le x \le 1.0$) nanoparticles. The reference patterns for cubic and tetragonal $CuFe_2O_4$ nanoparticles and reacting metal oxides are also included. The formation of the cubic spinel lattice with the *Fd3m* space group is confirmed by the characteristic diffractions corresponding to JCPDS card 77-0010. An exception is the $CuFe_{1.8}Al_{0.2}O_4$ sample that indicates the presence of unreacted oxides.

where λ is the wavelength of the X-rays and θ is the Bragg's angle. The interplanar spacing decreases from 2.512 Å for pure $CuFe_2O_4$ nanoparticles to 2.440 Å for $CuFeAlO_4$ nanoparticles, i.e. an increase in Al^{3+} doping reduces the interplanar spacing due to smaller ionic radius of Al^{3+} ions.

Table 2 – The structural properties[a] of $CuFe_{2-x}Al_xO_4$ ($0 \le x \le 1.0$) nanoparticles calculated from the X-ray diffraction (XRD) analysis.

Sample	M (g/mol)	a (Å)	V (Å^3)	d_{311} (Å)	ρ_{xrd} (g/cm^3)	D (nm)
$CuFe_2O_4$	239.4	8.397	592.2	2.532	5.371	26.33 ± 1.96
$CuFe_{1.8}Al_{0.2}O_4$	233.6	8.354	583.0	2.519	5.323	28.69 ± 1.38
$CuFe_{1.6}Al_{0.4}O_4$	227.8	8.271	565.8	2.494	5.349	35.16 ± 1.79
$CuFe_{1.4}Al_{0.6}O_4$	222.0	8.249	561.3	2.487	5.256	43.93 ± 2.33
$CuFe_{1.2}Al_{0.8}O_4$	216.2	8.144	540.2	2.456	5.318	32.03 ± 0.87
$CuFeAlO_4$	210.5	8.093	530.0	2.440	5.275	48.29 ± 1.72

[a] M: molecular weight; a: lattice parameter; V: volume; d_{311}: interplanar distance in (311) plane; ρ_{xrd}: X-ray density; D: crystallite size.

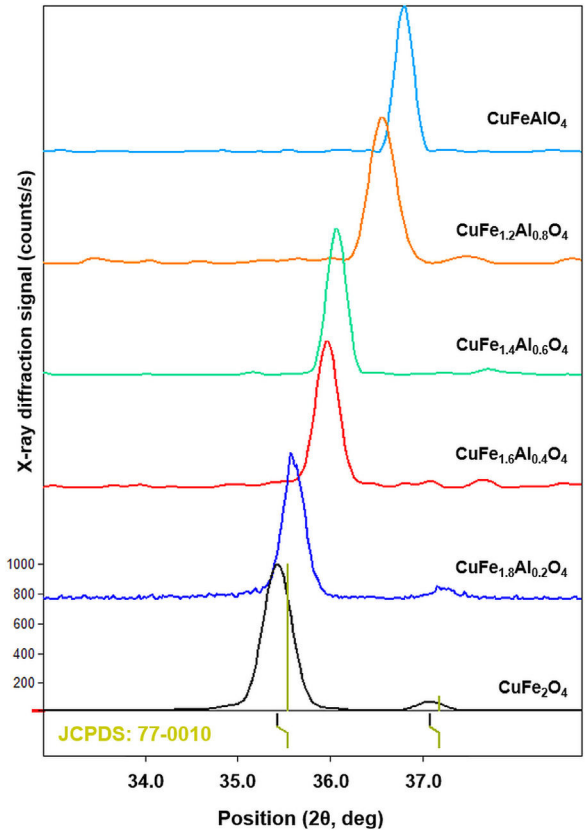

Fig. 3 – XRD patterns of the annealed $CuFe_{2-x}Al_xO_4$ ($0 \le x \le 1.0$) nanoparticles showing the position of characteristic (311) diffraction. The position of (311) peak varies with the increasing Al^{3+} content.

The lattice parameter can be calculated from the following Eq. (2):

$$a = d_{hkl}\sqrt{h^2 + k^2 + l^2} \tag{2}$$

where a is the lattice parameter of a cubic ($a = b = c$) lattice, and d_{hkl} is the interplanar spacing in the successive crystallographic planes (h, k, l) of the lattice. The lattice parameter of pure $CuFe_2O_4$ ($0 \le x \le 1$) nanoparticles is calculated as 8.397 Å that is comparable to the values reported in the literature [37,38]. Al^{3+} doped ferrites exhibit a decrease in the lattice parameter with the increasing Al^{3+} content that is again related to the differences in the ionic radii of Al^{3+} and Fe^{3+} ions. Quinzeni et al. [39] also demonstrated that at increasing Al^{3+} content, a more compact unit cell was formed with a smaller lattice parameter. Thus, $CuFeAlO_4$ nanoparticles show significantly smaller a value of 8.093 Å, as shown in Table 2.

Lattice volume (V) shows a similar trend along the series of $CuFe_{2-x}Al_xO_4$ ($0 \le x \le 1$) nanoparticles as it is calculated from the lattice parameter as ($V = a^3$). The lattice volume of $CuFe_{2-x}Al_xO_4$ ($0 \le x \le 1.0$) nanoparticles is reduced from 592.2 Å^3 to 530.0 Å^3 with the increasing Al^{3+} content. The density (ρ_{xrd}) of $CuFe_{2-x}Al_xO_4$ ($0 \le x \le 1.0$) nanoparticles can also be determined from the XRD analysis as given by the following equation (3) [33,40]:

$$p_{xrd} = \frac{8M}{N_A a^3} \tag{3}$$

where M is molecular weight and N_A is Avogadro's number. The density is a measure of mass per unit volume, while both molecular weight and lattice volume decrease with the addition of Al^{3+} ions as the dopant. However, the decrease in density is not uniform because it depends on the magnitude of the decrease of molecular weight and lattice volume. Hence, due to the different extent of decrease in lattice volume of thermally annealed $CuFe_{2-x}Al_xO_4$ ($0 \le x \le 1.0$) nanoparticles, the density does not follow a clear pattern and does not correlate with the Al^{3+} content.

The crystallite size (D) of the annealed $CuFe_{2-x}Al_xO_4$ ($0 \le x \le 1.0$) nanoparticles is determined by the Scherrer's formula [41], equation (4):

$$D = \frac{K\lambda}{B\cos\theta} \tag{4}$$

where K is a numerical factor ($K = 0.89$) referred to as the crystallite-shape factor and B is full-width at half-maximum of the diffraction peaks in radians. For the crystallite size calculations, three of the most intense diffraction peaks corresponding to (220), (311), and (440) planes are evaluated and the data are reported along with standard deviation in Table 2. Unlike the lattice parameter (a), the value of D in general increases from 26.33 nm to 48.29 nm with the increase in Al^{3+} dopant from ($x = 0 \rightarrow 1$). However, an exception is also recorded as $CuFe_{1.2}Al_{0.8}O_4$ nanoparticles exhibit small crystallite size (32.03 nm) compared to other samples. Nonetheless, the increase in crystallite size is attributed to the sample's tendency to fuse at high temperatures. The smaller, strained unit cells demonstrate a higher rate of sintering that leads to an increase in the crystallite size [42]. Thus, XRD analyses

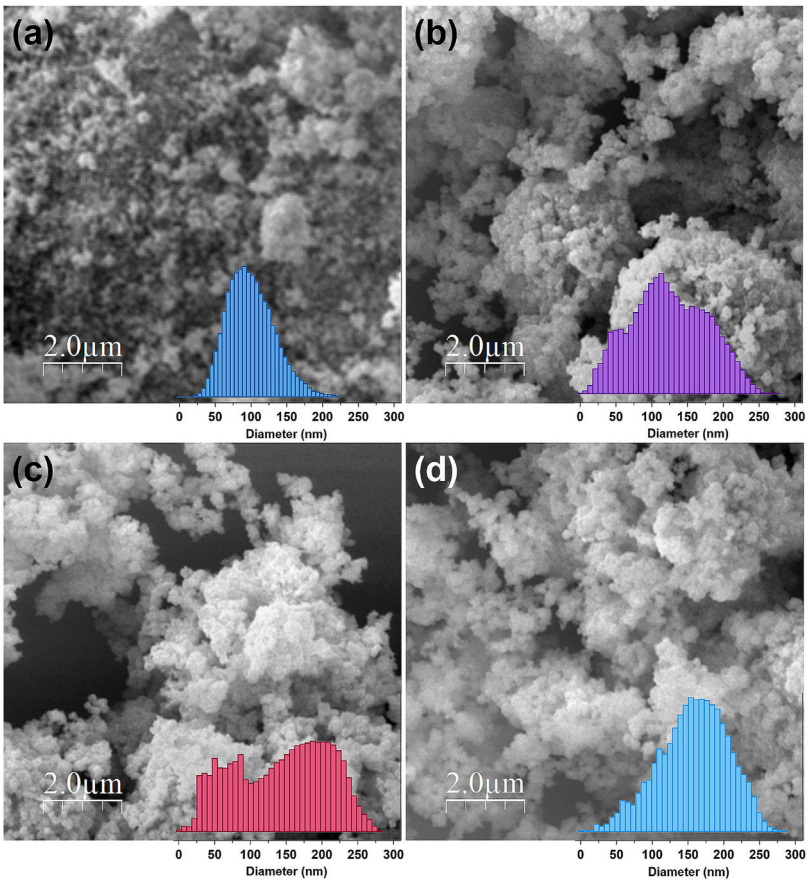

Fig. 4 – SEM images of (a) $CuFe_2O_4$, (b) $CuFe_{1.8}Al_{0.2}O_4$, (c) $CuFe_{1.4}Al_{0.6}O_4$, and (d) $CuFeAlO_4$ nanoparticles. The particle size distribution histograms obtained from the topographic analysis of the respective micrographs are shown as the insets.

provide significant information about the structural properties of $CuFe_{2-x}Al_xO_4$ ($0 \leq x \leq 1.0$) nanoparticles.

Morphology

The SEM images of the $CuFe_{2-x}Al_xO_4$ nanoparticles with ($x = 0.2$, 0.6, and 1.0) are shown in Fig. 4. Pure $CuFe_2O_4$ nanoparticles show a uniform microstructure with the smallest particle size and narrow size distribution, as shown in Fig. 4a. The micrographs of doped $CuFe_{2-x}Al_xO_4$ ($0 \leq x \leq 1$) nanoparticles show similar microstructure and surface morphology. The clusters of $CuFe_{2-x}Al_xO_4$ ($0 \leq x \leq 1$) nanoparticles can be seen in these micrographs (Fig. 4b–d). The respective histograms obtained via image analysis tools provide detailed insight into the microstructural differences among different types of $CuFe_{2-x}Al_xO_4$ ($0 \leq x \leq 1$) nanoparticles. Pure $CuFe_2O_4$ nanoparticles exhibit the smallest size and narrow size distribution compared to doped samples. The aggregate size of doped $CuFe_{2-x}Al_xO_4$ ($0 \leq x \leq 1$) nanoparticles increases with the Al^{3+} content. However, the size distribution in $CuFeAlO_4$ nanoparticles is narrow compared to $CuFe_{1.8}Al_{0.2}O_4$ and $CuFe_{1.4}Al_{0.6}O_4$ samples.

Further analysis of the micrographs and 3D imaging shows the surface topography and roughness. Fig. 5 shows 3D SEM images of the $CuFe_{2-x}Al_xO_4$ nanoparticles with ($x = 0$, 0.2, 0.6, and 1.0). The mean particle or aggregate size is calculated with an SEM image analysis program: ImageJ 1.52a by the National Institute of Health [21]. The mean particle sizes for $CuFe_2O_4$, $CuFe_{1.8}Al_{0.2}O_4$, $CuFe_{1.4}Al_{0.6}O_4$, and $CuFeAlO_4$ nanoparticles are 104.5, 126.2, 149.0, and 160.5 nm, respectively. Thus, mean particle or aggregate size increases with the increasing Al^{3+} content, and $CuFeAlO_4$ nanoparticles exhibit the highest values. This is attributed to the higher degree of sintering exhibited by the strained smaller lattices containing more Al^{3+} ions [42].

The chemical composition of $CuFe_{2-x}Al_xO_4$ ($0 \leq x \leq 1.0$) nanoparticles is determined from the EDS analysis. Fig. 6 shows a typical EDS spectrum of $CuFe_{1.4}Al_{0.6}O_4$ nanoparticles. The results of EDS analysis are given in Table 3, which compares theoretically calculated elemental percentage (at%) with the experimentally observed (at%) for the tested samples. The analyses reveal significant differences in the calculated and experimentally-found chemical composition of these samples. The major differences lie in the amount (at%) of oxygen that is significantly lower than the expected values, while the amount (at%) of metals (Cu, Fe, and Al) is generally higher than the theoretically calculated amount. This trend can be explained by the presence of oxygen vacancies in the annealed $CuFe_{2-x}Al_xO_4$ ($0 \leq x \leq 1.0$) nanoparticles. According to the literature [43–45], the loss of oxygen is inevitable during thermal annealing of oxides at temperatures above 700 °C and the concentration of oxygen vacancies generally increases with

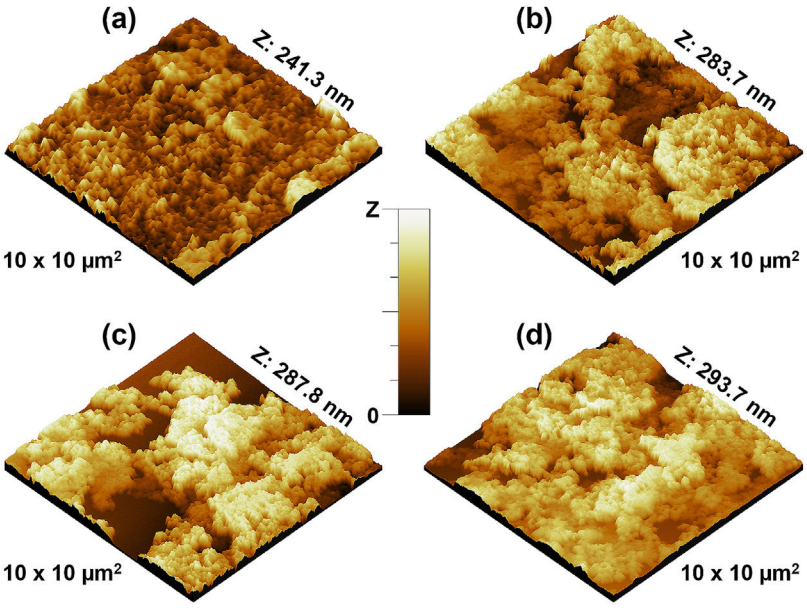

Fig. 5 – 3D micrographs of (a) $CuFe_2O_4$, (b) $CuFe_{1.8}Al_{0.2}O_4$, (c) $CuFe_{1.4}Al_{0.6}O_4$, and (d) $CuFeAlO_4$ nanoparticles.

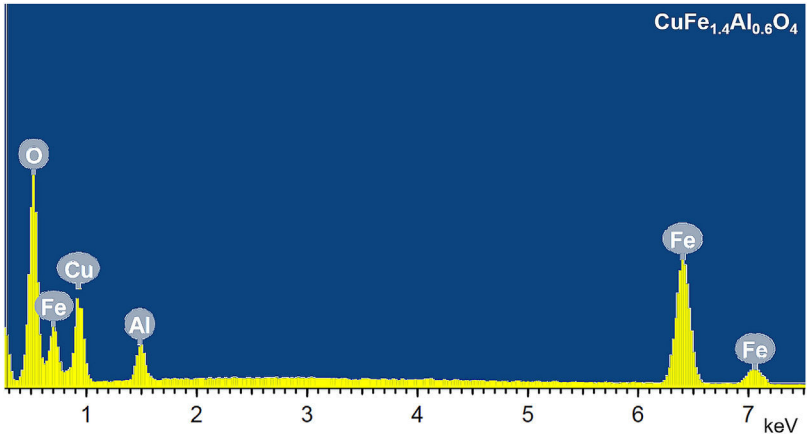

Fig. 6 – The EDS spectrum of the annealed $CuFe_{1.4}Al_{0.6}O_4$ nanoparticles.

the annealing temperature. Thus, $CuFe_{2-x}Al_xO_4$ $(0 \le x \le 1.0)$ nanoparticles annealed at 1000 °C reveal the formation of oxygen vacancies as indicated by the reduced amount (at%) of oxygen and an increased amount (at%) of metal ions (Cu^{2+}, Fe^{3+}, and Al^{3+}) compared to theoretically calculated values.

Photoluminescence study

The optical properties of the spinel $CuFe_{2-x}Al_xO_4$ $(0 \le x \le 1)$ nanoparticles are studied by examining their photoluminescence emissions at room temperature. The emission spectra reveal significant information about the excitation, immigration, and recombination of the photogenerated electron (e^-) and hole (h^+) pairs in a sample [46]. Fig. 7 shows the PL spectra of different $CuFe_{2-x}Al_xO_4$ $(0 \le x \le 1.0)$ nanoparticles excited at 254 nm. The PL emission spectra are deconvoluted into multiple Gaussian components to obtain the best-fit approximation of the experimental data, which indicates the surface defects and electronic structure of the sample. $CuFe_2O_4$ nanoparticles exhibit three major PL emissions: violet emission at 461.1 nm (2.69 eV), the most intense blue emissions at 485.9 nm (2.55 eV), and the least intense green emission at 518.2 nm (2.39 eV).

$CuFe_2O_4$ is inherently a low bandgap semiconductor. However, the bandgap energy depends on different factors such as the method of preparation, experimental conditions, annealing temperature and time, microstructure, and chemical composition that is why different values of the bandgap energy ranging from 1.32–3.09 eV have been reported in the literature for pure $CuFe_2O_4$ nanostructures [1,47–50]. Considering the structure and chemical composition of the annealed $CuFe_2O_4$ nanoparticles, the green emission (2.39 eV) is attributed to the band to band transitions. The violet and blue emissions are assigned to the luminescence centers that are formed by band edge free excitons, intra-bandgap lattice defects such as oxygen vacancies, and their aggregates [51,52].

Table 3 – The chemical composition of $CuFe_{2-x}Al_xO_4$ ($0 \le x \le 1.0$) nanoparticles: Theoretically calculated and experimentally obtained composition (in at%) of $CuFe_{2-x}Al_xO_4$ ($0 \le x \le 1$) nanoparticles with different Al^{3+}-dopant content.

Sample	Cu (at%)		Fe (at%)		Al (at%)		O (at%)	
	Calc.	Exp.	Calc.	Exp.	Calc.	Exp.	Calc.	Exp.
$CuFe_2O_4$	14.29	13.90	28.57	29.73	0.00	0.00	57.14	56.36
$CuFe_{1.8}Al_{0.2}O_4$	14.29	14.58	25.71	25.51	2.86	4.17	57.14	55.74
$CuFe_{1.4}Al_{0.6}O_4$	14.29	14.37	20.00	20.40	8.57	8.20	57.14	57.04
$CuFeAlO_4$	14.29	14.85	14.29	14.75	14.29	13.86	57.14	56.53

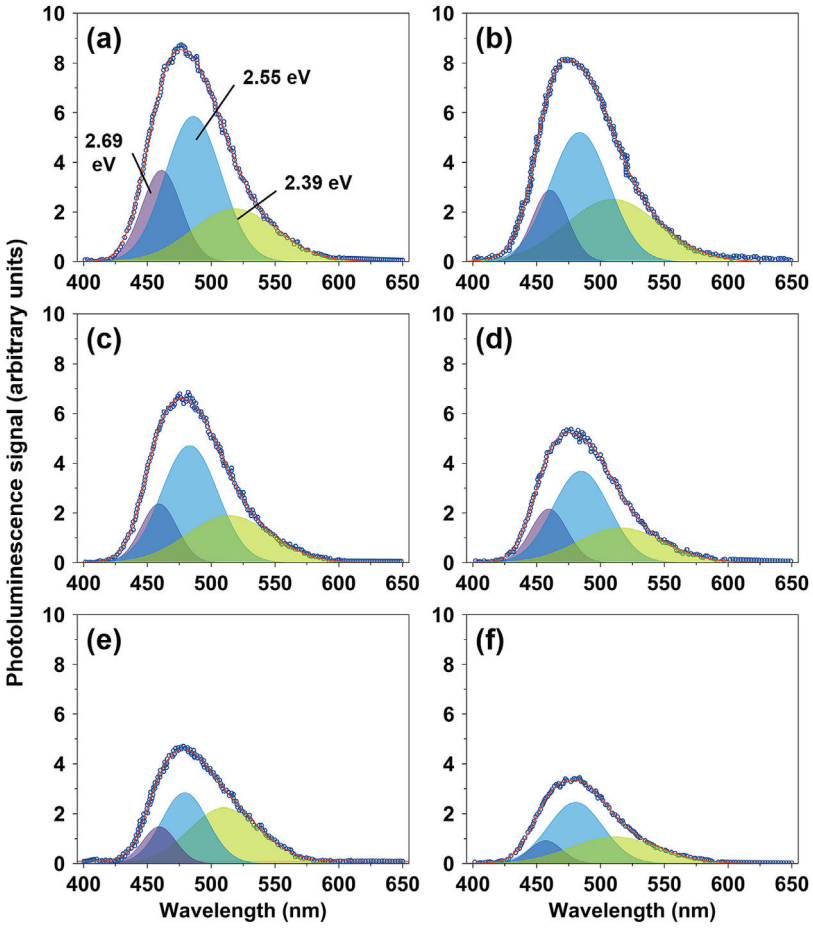

Fig. 7 – Photoluminescence spectra of the annealed $CuFe_{2-x}Al_xO_4$ ($0 \le x \le 1.0$) nanoparticles with different Al^{3+} content: (a) $CuFe_2O_4$, (b) $CuFe_{1.8}Al_{0.2}O_4$, (c) $CuFe_{1.6}Al_{0.4}O_4$, (d) $CuFe_{1.4}Al_{0.6}O_4$, (e) $CuFe_{1.2}Al_{0.8}O_4$, and (f) $CuFeAlO_4$ nanoparticles.

Raja et al. [51] observed the emission bands in the 410–460 nm region due to the intra-bandgap defects such as oxygen vacancies. Thus, violet emission (2.69 eV) is attributed to the lattice defects resulting from oxygen vacancies on the surface of $CuFe_2O_4$ nanoparticles. The blue emission (2.55 eV) is assigned to the transitions between the defect sites and valence band or between the conduction band and defect sites. Paramasivan et al. [53] also reported sharp emission bands (at approximately 460, 490, 550, and 590 nm) for hydrothermally-prepared $CuFe_2O_4$ nanoparticles annealed at 400–700 °C. Thus, these results are well in agreement with the literature [53–55], albeit there are peculiar differences in the emission spectrum of $CuFe_2O_4$ nanoparticles.

The emission wavelengths of $CuFe_{2-x}Al_xO_4$ nanoparticles with ($x = 0.4$, 0.6, and 1.0) do not change greatly by Al^{3+} doping, as shown in Fig. 7b–f. However, the luminescence signal is significantly reduced with the increasing Al^{3+} content. EDS results have already shown that like pure $CuFe_2O_4$, $CuFe_{2-x}Al_xO_4$ ($0 \le x \le 1$) nanoparticles are oxygen deficient. The decrease in luminescence signal of Al^{3+} doped $CuFe_{2-x}Al_xO_4$ ($0 \le x \le 1$) nanoparticles can be attributed to different factors: (a) increase in crystallite size, and (b) the lower rate of recombination of photoexcited (e^-) and (h^+). Other factors like the presence of impurities or secondary phases are not considered because of their absence or negligible presence in the XRD patterns of $CuFe_{2-x}Al_xO_4$ ($0 \le x \le 1$) nanoparticles.

Considering the effect of crystallite size, many researchers suggest that smaller particle size increases the quantum efficiency and should improve the luminescence signal due to the enhanced quantum confinement effect [56–58]. For example, Hjiri et al. [59] reveal that the differences in the crystallite size of $NiFe_2O_4$ nanoparticles influence the luminescence signal, i.e. an increase in crystallite size decreases the signal. However, Kombaiah et al. [60] argue that the smaller $CuFe_2O_4$ particle size means an increased number of dangling bonds combining with the oxygen vacancies, thereby creating non-radiative defects at the surface of nanoparticles and reducing the luminescence signal. The idea is supported by other researchers [49,61]. Therefore, a decrease in the luminescence signal of $CuFe_{2-x}Al_xO_4$ $(0 \le x \le 1)$ nanoparticles may not be due to the increase in their crystallite size compared to pure $CuFe_2O_4$. An evidence, in this regard, is presented by the $CuFe_{1.2}Al_{0.8}O_4$ nanoparticles with $D = 32.0$ nm (Fig. 7e) that shows lower photoluminescent intensity despite its smaller size compared to $CuFe_{1.4}Al_{0.6}O_4$ nanoparticles with $D = 43.9$ nm (Fig. 7d).

On the other hand, it is well known that photoluminescence results from the recombination of photogenerated charge carriers (e^-/h^+), and slower radiative recombination reduces the emission [62]. Therefore, we believe that lowering of the luminescence signal should be ascribed to the slower (e^-/h^+) recombination rate [13,46]; that is the direct recombination of excited electrons in Fe^{3+} conduction band with holes is prevented by Al^{3+} doping resulting in a lower signal. Al^{3+} acts as a surface trap for (e^-) and delays their recombination with (h^+); thereby reducing the luminescence signal. The dopant ions are known to improve the photocatalytic properties of various oxides by diminishing the rate of recombination and expanding the transition time of photoexcited charge carriers [62,63]. Therefore, the higher ratio of Al^{3+} in $CuFe_{2-x}Al_xO_4$ $(0 \le x \le 1)$ nanoparticles ensures greater charge separation and availability, which is essential for surface redox reactions. Consequently, $CuFe_{2-x}Al_xO_4$ $(0 \le x \le 1.0)$ nanoparticles have great potential for photocatalytic applications.

Conclusions

This study presents solid-state synthesis of $CuFe_{2-x}Al_xO_4$ $(0 \le x \le 1.0)$ nanoparticles using HEBM technique. $CuFe_{2-x}Al_xO_4$ $(0 \le x \le 1)$ nanoparticles synthesized at room temperature exhibit semicrystalline spinel structure, which transforms into single-phase cubic spinel lattice by annealing at 1000 °C. As the dopant (Al^{3+}) concentration increases, the annealed nanoparticles show an increase in crystallite size and particle diameter with narrow size distribution and reduced surface roughness. The smaller unit cells of Al^{3+}-doped nanoparticles show a higher degree of fusion and sintering tendency compared to pure $CuFe_2O_4$ nanoparticles. The photoluminescence spectra of $CuFe_{2-x}Al_xO_4$ $(0 \le x \le 1)$ nanoparticles reveal a decrease in the emission intensity with the increasing Al^{3+} content, which indicates the ability of dopant ions to slow down the recombination of (e^-) and (h^+). $CuFe_{2-x}Al_xO_4$ $(0 \le x \le 1)$ nanoparticles present greater charge availability for surface redox reactions that could potentially enhance their photocatalytic properties.

Authors' contributions

Conceptualization, F.A.A. and A.A.; methodology, F.A.A.; validation, F.A.A.; formal analysis, F.A.A. and M.A.; investigation, M.A. and F.A.; data curation, M.A., U.Y.Q., and F.A.; writing–original draft preparation, A.A.; writing–review and editing, U.Y.Q. and A.A.; visualization, U.Y.Q. and A.A.; project administration, F.A.A. and A.A.; funding acquisition, F.A.A. and A.A. All authors have read and agreed to the final version of the manuscript.

Funding

This research was funded by King AbdulAziz City for Science and Technology (KACST), grant number 13-NAN467-04.

Conflicts of interest

The authors declare no conflict of interest. The funders had no role in the design of the study; in the collection, analyses, or interpretation of data; in the writing of the manuscript, or in the decision to publish the results.

Acknowledgments

The authors would like to acknowledge the support provided by King AbdulAziz City for Science and Technology (KACST) through the Science and Technology Unit at King Fahd University of Petroleum and Minerals (KFUPM) for this work through project No.13-NAN467-04 as part of the National Science, Technology, and Innovation Plan. F.A.A. and A.A. are grateful to S.B. Waje and M.A. Atieh for their help in the characterization of samples and discussions of the outcomes.

REFERENCES

[1] E. Casbeer, V.K. Sharma, X.-Z. Li, Synthesis and photocatalytic activity of ferrites under visible light: a review, Sep. Purif. Technol. 87 (2012) 1–14, http://dx.doi.org/10.1016/j.seppur.2011.11.034.

[2] M. Estrella, L. Barrio, G. Zhou, X. Wang, Q. Wang, W. Wen, J.C. Hanson, A.I. Frenkel, J.A. Rodriguez, In situ characterization of $CuFe_2O_4$ and Cu/Fe_3O_4 water–gas shift catalysts, J. Phys. Chem. C 113 (2009) 14411–14417.

[3] K.-S. Kang, C.-H. Kim, K.-K. Bae, W.-C. Cho, W.-J. Kim, Y.-H. Kim, S.-H. Kim, C.-S. Park, Redox cycling of $CuFe_2O_4$ supported on ZrO_2 and CeO_2 for two-step methane reforming/water splitting, Int. J. Hydrogen Energy 35 (2010) 568–576.

[4] D. Yang, B. An, W. Wei, M. Jiang, J. You, H. Wang, A novel sustainable strategy for the synthesis of phenols by magnetic $CuFe_2O_4$-catalyzed oxidative hydroxylation of arylboronic acids under mild conditions in water, Tetrahedron 70 (2014) 3630–3634.

[5] B. Ren, Y. Huang, C. Han, M.N. Nadagouda, D.D. Dionysiou, Ferrites as photocatalysts for water splitting and degradation of contaminants, in: Ferrites and Ferrates: Chemistry and Applications in Sustainable Energy and Environmental Remediation, ACS Publications, 2016, pp. 79–112.

[6] V.K. Sharma, C. He, R. Doong, D.D. Dionysiou, Water depollution using ferrites photocatalysts, in: Green Materials for Energy, Products and Depollution, Springer, 2013, pp. 135–150.

[7] S. Hussain, S. Hussain, A. Waleed, M.M. Tavakoli, Z. Wang, S. Yang, Z. Fan, M.A. Nadeem, Fabrication of $CuFe_2O_4$/α-Fe_2O_3 composite thin films on FTO coated glass and 3-D nanospike structures for efficient photoelectrochemical water splitting, ACS Appl. Mater. Interfaces 8 (2016) 35315–35322.

[8] X. Li, A. Liu, D. Chu, C. Zhang, Y. Du, J. Huang, P. Yang, High performance of manganese porphyrin sensitized p-type $CuFe_2O_4$ photocathode for solar water splitting to produce hydrogen in a tandem photoelectrochemical cell, Catalysts 8 (2018) 108, http://dx.doi.org/10.3390/catal8030108.

[9] M. Tarek, K.M.R. Karim, S.M. Sarkar, A. Deb, H.R. Ong, H. Abdullah, C.K. Cheng, M.M.R. Khan, Hetero-structure CdS–$CuFe_2O_4$ as an efficient visible light active photocatalyst for photoelectrochemical reduction of CO_2 to methanol, Int. J. Hydrogen Energy 44 (2019) 26271–26284.

[10] K.M.R. Karim, M. Tarek, S.M. Sarkar, R. Mouras, H.R. Ong, H. Abdullah, C.K. Cheng, M.M.R. Khan, Photoelectrocatalytic reduction of CO_2 to methanol over $CuFe_2O_4$@ PANI photocathode, Int. J. Hydrogen Energy (2020).

[11] J. Wu, X. Wang, H. Kang, J. Zhang, C. Yang, $CuFe_2O_4$ as heterogeneous catalyst in degradation of p-nitrophenol with photoelectron-Fenton-like process, Int. J. Environ. Stud. 71 (2014) 534–545.

[12] X. Lei, M. You, F. Pan, M. Liu, P. Yang, D. Xia, Q. Li, Y. Wang, J. Fu, $CuFe_2O_4$@GO nanocomposite as an effective and recoverable catalyst of peroxymonosulfate activation for degradation of aqueous dye pollutants, Chin. Chem. Lett. 30 (2019) 2216–2220.

[13] M.R. Khan, M.R. Uddin, H. Abdullah, K.R. Karim, A. Yousuf, C.K. Cheng, H.R. Ong, Preparation and characterization of $CuFe_2O_4$/TiO_2 photocatalyst for the conversion of CO_2 into methanol under visible light, vol. 10, 2016, pp. 9.

[14] A.C. Nawle, A.V. Humbe, M.K. Babrekar, S.S. Deshmukh, K.M. Jadhav, Deposition, characterization, magnetic and optical properties of Zn doped $CuFe_2O_4$ thin films, J. Alloys Compd. 695 (2017) 1573–1582.

[15] K. Elayakumar, A. Manikandan, A. Dinesh, K. Thanrasu, K.K. Raja, R.T. Kumar, Y. Slimani, S.K. Jaganathan, A. Baykal, Enhanced magnetic property and antibacterial biomedical activity of Ce^{3+} doped $CuFe_2O_4$ spinel nanoparticles synthesized by sol–gel method, J. Magn. Magn. Mater. 478 (2019) 140–147.

[16] M.K.A. Kar, R. Fazaeli, F. Manteghi, M. Ghahari, Structural, optical, and isothermic studies of $CuFe_2O_4$ and Zn-doped $CuFe_2O_4$ nanoferrite as a magnetic catalyst for photocatalytic degradation of direct red 264 under visible light irradiation, Environ. Prog. Sustain. Energy 38 (2019) 13109, http://dx.doi.org/10.1002/ep.13109.

[17] C.C. Piras, S. Fernández-Prieto, W.M.D. Borggraeve, Ball milling: a green technology for the preparation and functionalisation of nanocellulose derivatives, Nanoscale Adv. 1 (2019) 937–947, http://dx.doi.org/10.1039/C8NA00238J.

[18] M. Satalkar, S.N. Kane, On the study of Structural properties and Cation distribution of $Zn_{0.75-x}Ni_xMg_{0.15}Cu_{0.1}Fe_2O_4$ nano ferrite: effect of Ni addition, J. Phys.: Conf. Ser. 755 (2016) 012050, http://dx.doi.org/10.1088/1742-6596/755/1/012050.

[19] A. Afzal, F.A. Abuilaiwi, R. Javaid, F. Ali, A. Habib, Solid-state synthesis of heterogeneous $Ni_{0.5}Cu_{0.5-x}Zn_xFe_2O_4$ spinel oxides with controlled morphology and tunable dielectric properties, J. Mater. Sci. Mater. Electron. 31 (2020) 14261–14270, http://dx.doi.org/10.1007/s10854-020-03982-8.

[20] I. Horcas, R. Fernández, J.M. Gómez-Rodríguez, J. Colchero, J. Gómez-Herrero, A.M. Baro, WSXM: a software for scanning probe microscopy and a tool for nanotechnology, Rev. Sci. Instrum. 78 (2007) 013705, http://dx.doi.org/10.1063/1.2432410.

[21] W. Rasband, ImageJ 1.52a: Image Processing and Analysis in Java, National Institute of Health, USA, 2020.

[22] J. Zheng, Z. Lin, W. Liu, L. Wang, S. Zhao, H. Yang, L. Zhang, One-pot synthesis of $CuFe_2O_4$ magnetic nanocrystal clusters for highly specific separation of histidine-rich proteins, J. Mater. Chem. B 2 (2014) 6207–6214, http://dx.doi.org/10.1039/C4TB00986J.

[23] S. Yang, C. Wu, H. Zhou, Y. Yang, Y. Zhao, C. Wang, W. Yang, J. Xu, An ullmann C–O coupling reaction catalyzed by magnetic copper ferrite nanoparticles, Adv. Synth. Catal. 355 (2013) 53–58, http://dx.doi.org/10.1002/adsc.201200600.

[24] C.V. Niveditha, M.J.J. Fatima, S. Sindhu, Comprehensive interfacial study of potentio-dynamically synthesized copper oxide thin films for photoelectrochemical applications, J. Electrochem. Soc. 163 (2016) H426, http://dx.doi.org/10.1149/2.0971606jes.

[25] X. Zhang, Y. Niu, X. Meng, Y. Li, J. Zhao, Structural evolution and characteristics of the phase transformations between α-Fe_2O_3, Fe_3O_4 and γ-Fe_2O_3 nanoparticles under reducing and oxidizing atmospheres, CrystEngComm 15 (2013) 8166–8172, http://dx.doi.org/10.1039/C3CE41269E.

[26] S. Kumar, R. Prakash, V. Kumar, A novel yellowish white Dy3+ activated α-Al_2O_3 phosphor: photoluminescence and optical studies, Funct. Mater. Lett. 08 (2015) 1550061, http://dx.doi.org/10.1142/S1793604715500617.

[27] V. Berbenni, A. Marini, C. Milanese, G. Bruni, Solid state synthesis of $CuFe_2O_4$ from $Cu(OH)_2{\cdot}CuCO_{3\text{-}4}FeC_2O_4{\cdot}2H_2O$ mixtures: mechanism of reaction and thermal characterization of $CuFe_2O_4$, J. Therm. Anal. Calorim. 99 (2010) 437–442, http://dx.doi.org/10.1007/s10973-009-0099-z.

[28] T.F. Marinca, I. Chicinaş, O. Isnard, Synthesis, structural and magnetic characterization of nanocrystalline $CuFe_2O_4$ as obtained by a combined method reactive milling, heat treatment and ball milling, Ceram. Int. 38 (2012) 1951–1957, http://dx.doi.org/10.1016/j.ceramint.2011.10.026.

[29] E.Z. Hegazy, I.H. Abd El-Maksod, A.M. Ibrahim, S.E.-S. El-Shafay, New insights about the formation of copper ferrite: in situ X-ray diffraction study, Bull. Natl. Res. Cent. 42 (2018) 9, http://dx.doi.org/10.1186/s42269-018-0010-9.

[30] M.A. Haija, A.F.S. Abu-Hani, N. Hamdan, S. Stephen, A.I. Ayesh, Characterization of H_2S gas sensor based on $CuFe_2O_4$ nanoparticles, J. Alloys Compd. 690 (2017) 461–468, http://dx.doi.org/10.1016/j.jallcom.2016.08.174.

[31] M.A. Ansari, A. Baykal, S. Asiri, S. Rehman, Synthesis and characterization of antibacterial activity of spinel chromium-substituted copper ferrite nanoparticles for biomedical application, J. Inorg. Organomet. Polym. 28 (2018) 2316–2327, http://dx.doi.org/10.1007/s10904-018-0889-5.

[32] V. Manikandan, A. Vanitha, E. Ranjith Kumar, J. Chandrasekaran, Effect of In substitution on structural, dielectric and magnetic properties of $CuFe_2O_4$ nanoparticles, J. Magn. Magn. Mater. 432 (2017) 477–483, http://dx.doi.org/10.1016/j.jmmm.2017.02.030.

[33] M.M. Naik, H.S.B. Naik, G. Nagaraju, M. Vinuth, K. Vinu, S.K. Rashmi, Effect of aluminium doping on structural, optical, photocatalytic and antibacterial activity on nickel ferrite nanoparticles by sol–gel auto-combustion method, J. Mater. Sci. Mater. Electron. 29 (2018) 20395–20414, http://dx.doi.org/10.1007/s10854-018-0174-y.

[34] P.N. Anantharamaiah, P.A. Joy, Effect of size and site preference of trivalent non-magnetic metal ions (Al3$\mathplus$, Ga3$\mathplus$, In3$\mathplus$) substituted for Fe3$\mathplus$on the magnetostrictive properties of sintered CoFe2O4, J. Phys. D: Appl. Phys. 50 (2017) 435005, http://dx.doi.org/10.1088/1361-6463/aa8af6.

[35] W.H. Bragg, W.L. Bragg, The reflection of X-rays by crystals, Proc. R. Soc. Lond. Ser. A Contain. Pap. Math. Phys. Charact. 88 (1913) 428–438, http://dx.doi.org/10.1098/rspa.1913.0040.
[36] J.M. Cowley, Diffraction Physics, 3rd ed., Elsevier, North Holland, 1995, http://dx.doi.org/10.1016/B978-0-444-82218-5.X5000-7.
[37] R. Köferstein, T. Walther, D. Hesse, S.G. Ebbinghaus, Crystallite-growth, phase transition, magnetic properties, and sintering behaviour of nano-$CuFe_2O_4$ powders prepared by a combustion-like process, J. Solid State Chem. 213 (2014) 57–64, http://dx.doi.org/10.1016/j.jssc.2014.02.010.
[38] M.K. Satheeshkumar, E.R. Kumar, C. Srinivas, G. Prasad, S.S. Meena, I. Pradeep, N. Suriyanarayanan, D.L. Sastry, Structural and magnetic properties of $CuFe_2O_4$ ferrite nanoparticles synthesized by cow urine assisted combustion method, J. Magn. Magn. Mater. 484 (2019) 120–125.
[39] I. Quinzeni, V. Berbenni, D. Capsoni, M. Bini, Ca- and Al-doped $ZnFe_2O_4$ nanoparticles as possible anode materials, J. Solid State Electrochem. 22 (2018) 2013–2024, http://dx.doi.org/10.1007/s10008-018-3901-7.
[40] C. Dun, G. Xi, X. Heng, Y. Zhang, Y. Liu, X. Xing, Comparative study on the magnetostrictive property of cobalt ferrite synthesized by different methods from spent Li-ion batteries, Ceram. Int. 45 (2019) 8539–8545, http://dx.doi.org/10.1016/j.ceramint.2019.01.170.
[41] U. Holzwarth, N. Gibson, The Scherrer equation versus the "Debye–Scherrer equation", Nat. Nanotech. 6 (2011) 534, http://dx.doi.org/10.1038/nnano.2011.145.
[42] L.d.S. Aguilera, R.L.S.B. Marçal, J.B. de Campos, M.H.P. da Silva, A.B.-H.d.S. FigueiredoS, Magnetic filter produced by $ZnFe_2O_4$ nanoparticles using freeze casting, J. Mater. Res. Technol. 7 (2018) 350–355, http://dx.doi.org/10.1016/j.jmrt.2018.04.012.
[43] J. Zheng, J. Xiao, J.-G. Zhang, The roles of oxygen non-stoichiometry on the electrochemical properties of oxide-based cathode materials, Nano Today 11 (2016) 678–694, http://dx.doi.org/10.1016/j.nantod.2016.08.011.
[44] J. Zhang, H. Bai, Y. Han, F. Wang, S. He, P. Liu, X. Zhang, H. Yuan, Z. Zhang, The effect of $CuFe_2O_4$ ferrite phase evolution on 3–5 μm waveband emissivity, Ceram. Int. 46 (2020) 7694–7702, http://dx.doi.org/10.1016/j.ceramint.2019.11.272.
[45] H. Gao, H. Yang, G. Yang, S. Wang, Effects of oxygen vacancy and sintering temperature on the photoluminescence properties and photocatalytic activity of CeO_2 nanoparticles with high uniformity, Mater. Technol. 33 (2018) 321–332, http://dx.doi.org/10.1080/10667857.2018.1438222.
[46] J.Y. Shen, Z.S. Cui, Z.W. Wu, J.X. Wang, Q. Ning, X.M. Lü, Simple preparation of $CuFe_2O_4/C_3N_4$ composites: characterisation and enhanced photocatalysis, Mater. Res. Innov. 19 (2015) 187–191, http://dx.doi.org/10.1179/1433075X14Y. 0000000240.
[47] R.K. Selvan, C.O. Augustin, V. Šepelák, L.J. Berchmans, C. Sanjeeviraja, A. Gedanken, Synthesis and characterization of $CuFe_2O_4/CeO_2$ nanocomposites, Mater. Chem. Phys. 112 (2008) 373–380, http://dx.doi.org/10.1016/j.matchemphys.2008.05.094.
[48] J. Kurian, M.J. Mathew, Structural, optical and magnetic studies of $CuFe_2O_4$, $MgFe_2O_4$ and $ZnFe_2O_4$ nanoparticles prepared by hydrothermal/solvothermal method, J. Magn. Magn. Mater. 451 (2018) 121–130, http://dx.doi.org/10.1016/j.jmmm.2017.10.124.
[49] S.S. Selima, M. Khairy, M.A. Mousa, Comparative studies on the impact of synthesis methods on structural, optical, magnetic and catalytic properties of $CuFe_2O_4$, Ceram. Int. 45 (2019) 6535–6540, http://dx.doi.org/10.1016/j.ceramint.2018.12.146.
[50] S. Singh, B.C. Yadav, R. Prakash, B. Bajaj, J.R. lee, Synthesis of nanorods and mixed shaped copper ferrite and their applications as liquefied petroleum gas sensor, Appl. Surf. Sci. 257 (2011) 10763–10770, http://dx.doi.org/10.1016/j.apsusc.2011.07.094.
[51] G. Raja, S. Gopinath, R.A. Raj, A.K. Shukla, M.S. Alhoshan, K. Sivakumar, Comparative investigation of $CuFe_2O_4$ nano and microstructures for structural, morphological, optical and magnetic properties, Phys. E: Low-Dimens. Syst. Nanostruct. 83 (2016) 69–73, http://dx.doi.org/10.1016/j.physe.2016.04.019.
[52] H.Y. Hafeez, S.K. Lakhera, P. Karthik, M. Anpo, B. Neppolian, Facile construction of ternary $CuFe_2O_4$-TiO2 nanocomposite supported reduced graphene oxide (rGO) photocatalysts for the efficient hydrogen production, Appl. Surf. Sci. 449 (2018) 772–779, http://dx.doi.org/10.1016/j.apsusc.2018.01.282.
[53] P. Paramasivan, P. Venkatesh, Controllable synthesis of $CuFe_2O_4$ nanostructures through simple hydrothermal method in the presence of thioglycolic acid, Phys. E: Low-Dimens. Syst. Nanostruct. 84 (2016) 258–262, http://dx.doi.org/10.1016/j.physe.2016.05.037.
[54] K.J. Kim, J.H. Lee, S.H. Lee, Magneto-optical investigation of spinel ferrite $CuFe_2O_4$: observation of Jahn–Teller effect in Cu^{2+} ion, J. Magn. Magn. Mater. 279 (2004) 173–177, http://dx.doi.org/10.1016/j.jmmm.204.01.078.
[55] G.F. Goya, H.R. Rechenberg, J.Z. Jiang, Structural and magnetic properties of ball milled copper ferrite, J. Appl. Phys. 84 (1998) 1101–1108, http://dx.doi.org/10.1063/1.368109.
[56] T. Takagahara, K. Takeda, Theory of the quantum confinement effect on excitons in quantum dots of indirect-gap materials, Phys. Rev. B 46 (1992) 15578.
[57] L. Vayssieres, C. Sathe, S.M. Butorin, D.K. Shuh, J. Nordgren, J. Guo, One-dimensional quantum-confinement effect in α-Fe_2O_3 ultrafine nanorod arrays, Adv. Mater. 17 (2005) 2320–2323.
[58] R. Das, G.G. Khan, S. Varma, G.D. Mukherjee, K. Mandal, Effect of quantum confinement on optical and magnetic properties of Pr–Cr-codoped bismuth ferrite nanowires, J. Phys. Chem. C 117 (2013) 20209–20216.
[59] M. Hjiri, N.H. Alonizan, M.M. Althubayti, S. Alshammari, H. Besbes, M.S. Aida, Preparation and photoluminescence of $NiFe_2O_4$ nanoparticles, J. Mater. Sci. Mater. Electron. 30 (2019) 15379–15387, http://dx.doi.org/10.1007/s10854-019-01914-9.
[60] K. Kombaiah, J.J. Vijaya, L.J. Kennedy, M. Bououdina, B. Al-Najar, Conventional and microwave combustion synthesis of optomagnetic $CuFe_2O_4$ nanoparticles for hyperthermia studies, J. Phys. Chem. Solids 115 (2018) 162–171, http://dx.doi.org/10.1016/j.jpcs.2017.12.024.
[61] A.A. Zarandi, A.A.S. Alvani, R. Salimi, H. Sameie, S. Moosakhani, D. Poelman, F. Rosei, Self-organization of an optomagnetic $CoFe_2O_4$–ZnS nanocomposite: preparation and characterization, J. Mater. Chem. C 3 (2015) 3935–3945.
[62] S. Irfan, L. Li, A.S. Saleemi, C.-W. Nan, Enhanced photocatalytic activity of La^{3+} and Se^{4+} co-doped bismuth ferrite nanostructures, J. Mater. Chem. A 5 (2017) 11143–11151.
[63] R. Sharma, M. Khanuja, S.N. Sharma, O.P. Sinha, Reduced band gap & charge recombination rate in Se doped α-Bi_2O_3 leads to enhanced photoelectrochemical and photocatalytic performance: Theoretical & experimental insight, Int. J. Hydrogen Energy 42 (2017) 20638–20648, http://dx.doi.org/10.1016/j.ijhydene.2017.07.011.